

Localization of vibrational modes in high-entropy oxides

C. M. Wilson,* R. Ganesh, and D. A. Crandles

Department of Physics, Brock University, St. Catharines, Ontario L2S 3A1, Canada

(Dated: October 16, 2023)

The recently-discovered high-entropy oxides offer a paradoxical combination of crystalline arrangement and high disorder. They differ qualitatively from established paradigms for disordered solids such as glasses and alloys. In these latter systems, it is well known that disorder induces localized vibrational excitations. In this article, we explore the possibility of disorder-induced localization in $\text{Mg}_{0.2}\text{Co}_{0.2}\text{Ni}_{0.2}\text{Cu}_{0.2}\text{Zn}_{0.2}\text{O}$, the prototypical high-entropy oxide with rock-salt structure. To describe phononic excitations, we model the interatomic potentials for the cation-oxygen interactions by fitting to the physical properties of the parent binary oxides. We validate our model against the experimentally determined crystal structure, bond lengths, and optical conductivity. The resulting phonon spectrum shows wave-like propagating modes at low energies and localized modes at high energies. Localization is reflected in signatures such as participation ratio and correlation amplitude. Finally, we explore the possibility of increased mass disorder in the oxygen sublattice. Admixing sulphur or tellurium atoms with oxygen enhances localization. It even leads to localized modes in the middle of the spectrum. Our results suggest that high-entropy oxides are a promising platform to study Anderson localization of phonons.

I. INTRODUCTION

The field of high-entropy oxides began with the synthesis of $\text{Mg}_{0.2}\text{Co}_{0.2}\text{Ni}_{0.2}\text{Cu}_{0.2}\text{Zn}_{0.2}\text{O}$ (hereafter referred to as HEO) by C. M. Rost *et al.* in 2015 [1]. The five parent binary oxides have limited mutual solid solubility and even differ in their crystal structures. Nevertheless, Rost *et al.* showed that HEO crystallizes in the rocksalt ($F\bar{m}3m$) structure [1] with a lattice constant $a = 4.236(1)$ Å [2]. The oxygen sublattice is ordered, while the cation sublattice is uniformly occupied by Mg, Co, Ni, Cu, and Zn with no observable short-range ordering at an atomic resolution of 1–3 Å [3]. A possible instance of the HEO crystal structure is shown schematically in Figure 1. Due to their low thermal conductivity/elastic modulus [4] and high Li-ion room temperature conductivity [5], high-entropy oxides are attractive candidates for thermal coatings [4] and solid-state batteries [5].

As disordered media do not have translational symmetry, phonon excitations cannot be associated with specific wavevectors. Likewise, there is no conventional classification of modes as longitudinal/transverse or acoustic/optical, although these notions can be suitably extended [6, 7]. In the context of glasses, Allen and Feldman [8] and Allen *et al.* [9] proposed a new taxonomy, with phonons classified as propagons, diffusons and locons. Propagons are extended, plane-wave-like excitations which generally occupy the low-frequency part of the vibrational density-of-states (VDOS). Within a propagon mode, atomic displacements are spatially coherent; *i.e.* nearest-neighbours tend to vibrate in the same direction. Diffusons occur in the middle region of the VDOS, with components that are randomly-oriented.

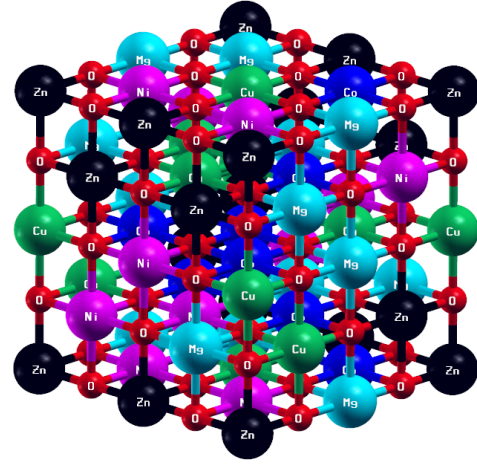


FIG. 1. Possible disorder realization of the $\text{Mg}_{0.2}\text{Co}_{0.2}\text{Ni}_{0.2}\text{Cu}_{0.2}\text{Zn}_{0.2}\text{O}$ crystal structure.

While they are spatially extended, a wavepacket of diffusons transports vibrational energy diffusively. Locons appear at high frequencies, above a ‘mobility-edge’ [9]. They exhibit randomly-oriented displacements that are localized over a small cluster of atoms.

The scaling theory of localization [10] predicts that all eigenstates of a one- or two-dimensional system become exponentially localized when any amount of disorder is added to an otherwise clean system. In three-dimensions, eigenstates may be localized or extended, depending upon the amount of disorder present in the system. This physics has been seen in the vibrational excitations of amorphous solids such as α -silicon.

The disorder in amorphous systems is structural in character. This may be contrasted with mass- and spring-constant-disorder in systems such as high-entropy alloys – a family of materials with atoms of metallic elements randomly distributed on a background lattice [11].

* cw14mi@brocku.ca

However, as alloys are typically electrically conducting, the physics of phonon localization is complicated by the inevitable presence of electron-phonon coupling. High-entropy oxides offer an attractive alternative. They possess a high degree of mass and spring-constant disorder. At the same time, they are electrically insulating with a large gap to electronic excitations. This makes for a relatively clean platform to study the localization of vibrational modes.

This paper is organized as follows: in Sec. II A, details of the classical lattice dynamics simulations are discussed. Sec. II B presents our model for $\text{Mg}_{0.2}\text{Co}_{0.2}\text{Ni}_{0.2}\text{Cu}_{0.2}\text{Zn}_{0.2}\text{O}$ and discusses refinements over previous approaches. Sec. II C compares the simulated crystal structure, bond lengths, and optical conductivity of HEO to experiment. Sec. III A characterizes the vibrational modes in terms of the relative amplitude [12], phase quotient [13], and polarization. Sec. III B presents several diagnostics for mode localization which suggest that locons do indeed exist in HEO beyond a high-frequency mobility edge in the VDOS.

II. MODEL, VALIDATION, AND METHODS

A. Methods

We use the **General Utility Lattice Program** (GULP) [14] to find the equilibrium structure and to evaluate the vibrational spectrum. This program is known to reproduce experimental structure and phonon band structure for ionic solids such as MgO and ZnO [15]. It takes into account Coulomb interactions as well as short-ranged forces. Supercells of HEO containing up to 8000 atoms were generated by uniformly distributing equiatomic proportions of Mg, Co, Ni, Cu, and Zn throughout the cation sublattice.

B. Model

The effects of polarizability were included with the shell model introduced by Dick and Overhauser [16], wherein atoms are divided into massive point charges bonded by harmonic springs to massless, charged shells; *i.e.* a core-shell pair interact through a potential

$$\Phi = \frac{1}{2} k r_{cs}^2, \quad (1)$$

where k is the stiffness constant and r_{cs} is the core-shell distance. For simplicity, the sum of the shell charge Y and the core charge was fixed to the formal charge on each ion, either +2 for cations or -2 for oxygens. The short-range shell-shell interactions were parameterized by the Buckingham potential

$$\Phi = A_{bb'} \exp\left(-\frac{|b-b'|}{\rho_{bb'}}\right) - \frac{C_{bb'}}{|b-b'|^6}, \quad (2)$$

where b, b' are internal atomic coordinates and the two terms on the right-hand side represent, respectively, the repulsion between electron clouds and the van-der-Waals attraction. In addition to Eqs. 1 and 2, the Coulomb potential also acts between all pairs of cores and shells.

Lewis and Catlow [17] observed reasonable agreement between the simulated and experimental elastic constants of spinel oxides by a) transferring the potential parameters directly from the parent binary oxides; b) neglecting cation-cation interactions, and; c) setting $C_{bb'} = 0$ for all interactions except oxygen-oxygen [18]. To reduce the number of free parameters, we make the same assumptions about HEO and use the Lewis and Catlow oxygen-oxygen potential without modification. GULP was then used to determine the remaining unknown parameters $\{Y, k, A, \rho\}$ by performing a relaxed fit to the parent binary oxides' experimental crystal structures, dielectric constants, and phonon frequencies. The final values of the parameters are listed in Tables I and II. Following Popov *et al.*, two Buckingham potentials operating over different distance ranges were used to model Cu-O interactions [19].

In Sec. III B 1, we discuss two hypothetical materials: 'high-entropy sulfide oxide' (HESO) and 'high-entropy telluride oxide' (HETeO). They are generated by randomly substituting half of the oxygen sublattice in HEO with sulfur and tellurium ions. As a minimal model for HESO, we take the cation-sulfur potential to be identical to the cation-oxygen potential. Likewise, we take the sulfur-sulfur and sulfur-oxygen potentials to be identical to the oxygen-oxygen potential. The sulfur and oxygen shell model parameters are also taken to be the same. Analogous assumptions are made for HETeO. These assumptions amount to increasing the mass disorder in HEO, but not the spring-constant disorder. HESO and HETeO have not been experimentally realized, although a high-entropy oxyfluoride has recently been synthesized [20].

TABLE I. Buckingham shell-shell parameters. The potentials operate over a distance range specified in the rightmost two columns.

	A (eV)	ρ (\AA^{-1})	C (eV/ \AA^6)	r_{min} (\AA)	r_{max} (\AA)
O-O	22764	0.149	27.88	0	12
Mg-O	1266.7	0.301	0	0	8
Co-O	1244.3	0.305	0	0	8
Ni-O	1794.8	0.283	0	0	8
Cu-O	2054.7	0.269	0	0	2.3
	558.23	0.360	0	2.3	8
Zn-O	571.82	0.353	0	0	8

C. Model validation

We next compare results from the GULP model to known experimental quantities to validate our model. In

TABLE II. Shell model parameters.

Ion	Y (e)	k ($eV \text{ \AA}^{-2}$)
O	-2.88	70.52
Mg	2.77	137.3
Co	3.20	66.51
Ni	3.68	95.48
Cu	3.82	85.37
Zn	2.19	19.19

the following discussion, all GULP results were averaged over fifty 4096-atom disorder realizations before comparing with results from literature.

1. Crystal structure

The HEO lattice parameters obtained from our model are listed in Table III. The cell angles are all correctly equal to 90° within error, and the cell lengths are in pairwise agreement. The cell lengths are slightly lower than XRD values (by $\sim 0.03 \text{ \AA}$ or 1%). Our results can be compared with Anand *et al.* [21], a theoretical study where cation-oxygen potentials developed by Lewis and Catlow [17] were applied to HEO. This study reports an even shorter cell length of 4.16 \AA . This suggests that our model, with its refinements, is closer to true HEO.

TABLE III. Crystal structure of HEO. The lattice parameter from [21] is taken to be twice the average cation-oxygen spacing of 2.08 \AA .

	XRD [2]	Anand <i>et al.</i> [21]	This work
α ($^\circ$)	90	–	90.000(2)
β ($^\circ$)	90	–	90.000(2)
γ ($^\circ$)	90	–	90.000(2)
a (\AA)	4.236(1)	4.16	4.2064(3)
b (\AA)	4.236(1)	4.16	4.2062(3)
c (\AA)	4.236(1)	4.16	4.2063(3)

2. Bond lengths

The distributions of nearest-neighbour cation-oxygen spacings (bond lengths) are presented in Figure 2. All distributions are composed of a main peak and a shoulder in the right tail. This can be compared with Anand *et al.* [21] which reports a bimodal distribution of Cu–O bonds in HEO and concluded that the experimentally-observed local lattice distortion around the Cu ions is due to a combination of the Jahn-Teller effect [22] and differences in ionic radii. The median bond lengths are listed explicitly in Table IV and are compared to results from EXAFS. Our results are in agreement with the experiment of Sushil *et al.* [23].

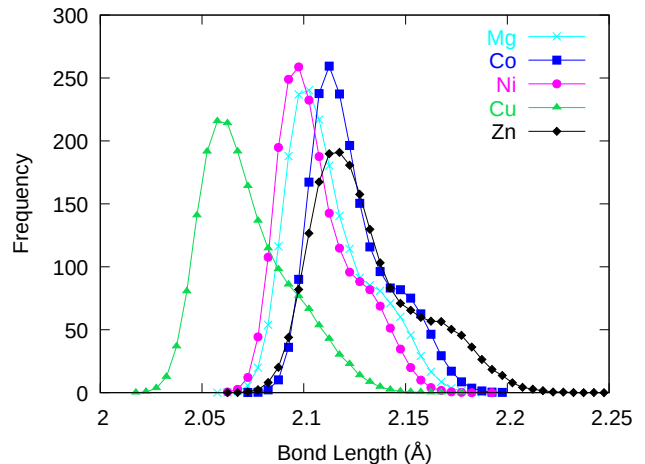


FIG. 2. Distribution of nearest-neighbour cation-oxygen spacings (bond lengths) in HEO. The solid lines are guides to the eye.

3. Optical conductivity

Afsharvosoughi and Crandles [2] measured the infrared reflectance of HEO and extracted the real optical conductivity $\sigma'(\omega)$ from Kramers-Kronig analysis [2]. Their data is reproduced in Fig. 3. Observe that $\sigma'(\omega)$ consists of a strong mode near 360 cm^{-1} and a weak mode at 160 cm^{-1} . The strong mode was identified with the reststrahlen band characteristic of rocksalt crystals. The weak mode is of yet unclear origin.

Figure 3 compares the optical conductivity from GULP to experiment. Our model successfully reproduces the weak mode and provides satisfactory agreement with the reststrahlen band.

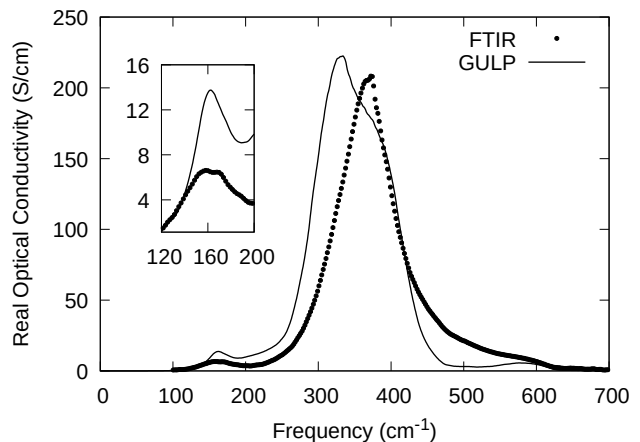


FIG. 3. Optical conductivity of HEO. Experimental FTIR (Fourier-transform infrared) data at 300 K adapted from [2]. This data is compared against the result from GULP based on our model.

TABLE IV. Median bond lengths in HEO. Rost *et al.* and Sushil *et al.* are EXAFS studies. Mg–O bonds were not analysed due to insufficient energy resolution. Rost *et al.* and Sushil *et al.* report two bond lengths for Cu–O, reflecting local Jahn-Teller distortions. The values cited in the table are averages, weighted by the number of bonds with each length. The error estimates from [21] are one-half the widths of the data points obtained by digitizing their Fig. 4a).

	Rost <i>et al.</i> [24]	Sushil <i>et al.</i> [23]	Anand <i>et al.</i> [21]	This work
Mg–O	–	–	2.088(3)	2.11(2)
Co–O	2.089(9)	2.0906	2.093(3)	2.12(2)
Ni–O	2.084(5)	2.0918	2.080(3)	2.10(2)
Cu–O	2.07(5)	2.0733	2.033(3)	2.07(2)
Zn–O	2.078(9)	2.0984	2.094(3)	2.12(3)

III. RESULTS

A. Mode characterization

In this section the vibrational modes in HEO are characterized in terms of their phase quotient, relative amplitude, and eigenvector polarization. All results are shown for a single 4096-atom disorder realization.

1. Relative amplitude

Carvalho *et al.* define the relative amplitude A of ionic species B as [12]

$$A(B; \omega_s) = \sum_{b \in B} \sum_{\alpha} |\varepsilon_{\alpha}(b; s)|^2 \quad (3)$$

where $\varepsilon_{\alpha}(b; s)$ is the projection of the s th eigenvector onto the b th atom in the α th Cartesian direction. The summation $\sum_{b \in B}$ extends over all atoms $\{b\}$ belonging to the species B . If the atomic motion in mode s is dominated by atoms in B then $A(B; \omega_s) \sim 1$; conversely, if the vibrations due to species B are weak then $A(B; \omega_s) \ll 1$. Note that $\sum_B A(B; \omega_s) = \sum_{b\alpha} |\varepsilon_{\alpha}(b; s)|^2 = 1$ by the orthonormality of the vibrational eigenvectors [25].

Figure 4 shows the relative amplitudes of the six ionic species in HEO. Observe that A is large for the heavier cations at low frequency; as frequency increases the cationic amplitudes fall while the oxygen amplitude rises to a maximum near 500 cm^{-1} . A transition from cation- to oxygen-dominated motion occurs near 300 cm^{-1} , where the amplitudes cross. Note that the Zn (oxygen) amplitude reaches a global maximum (minimum) near 150 cm^{-1} . It is reasonable to conclude that the smaller peak in the optical conductivity (Fig. 3) is caused by low-frequency oscillations of Zn ions against a stationary oxygen sublattice.

2. Phase quotient

The phase quotient introduced by Bell and Hibbins-Butler [7] generalizes the notions of acoustic/optical

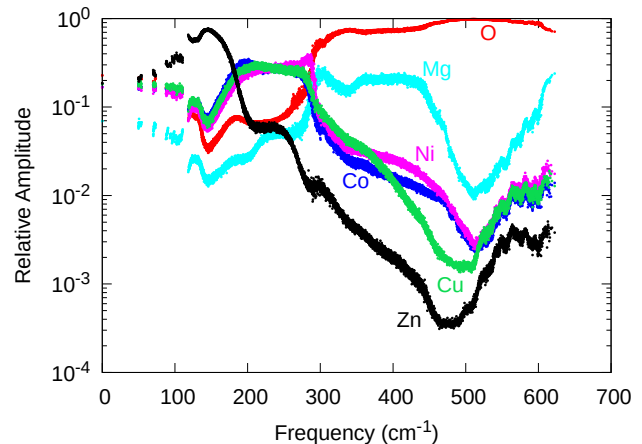


FIG. 4. Relative amplitudes in HEO.

phonons to disordered media. It is defined by

$$\phi(\omega_s) = \frac{\sum_{\langle bb' \rangle} \sum_{\alpha} \varepsilon_{\alpha}(b; s) \varepsilon_{\alpha}(b'; s)}{\sum_{\langle bb' \rangle} |\sum_{\alpha} \varepsilon_{\alpha}(b; s) \varepsilon_{\alpha}(b'; s)|} \quad (4)$$

where the summation $\sum_{\langle bb' \rangle}$ extends over all nearest-neighbours $\{b'\}$ of b . If $\phi(\omega_s) = +1$ nearest-neighbours vibrate in-phase and the vibrations are acoustic-like; if $\phi(\omega_s) = -1$ nearest-neighbours vibrate out-of-phase and the vibrations are optical-like.

The phase quotient of HEO is shown by the series marked ‘1NN’ in Fig. 5. As in ordered solids, the vibrations are highly acoustic-like at low frequency, near the Goldstone modes. As frequency increases, a transition to optical-like modes occurs. The peak near 500 cm^{-1} coincides with the maximum (minima) of the oxygen (cation) relative amplitudes in Fig. 4. Since Fig. 4 implies that it is only oxygen that moves at 500 cm^{-1} , the phase quotient is close to zero there, ‘midway’ between acoustic and optical vibrations.

Figure 5 also presents modified phase quotients with the summation over $\{b'\}$ restricted to nearest-neighbours in the cation/oxygen sublattices separately. Interestingly, the phase quotient within the oxygen sublattice peaks at 300 cm^{-1} where we see a transition from cation- to oxygen-dominated motion.

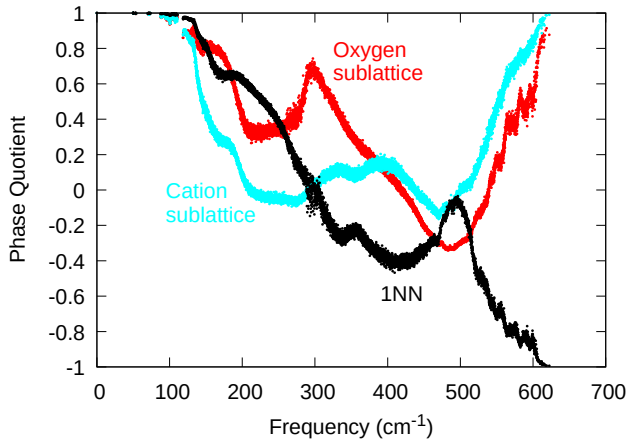


FIG. 5. Phase quotient of HEO. The curves marked ‘sublattice’ are calculated within a species-sublattice, *i.e.* with the summation over $\{b'\}$ in Eq. 4 restricted to nearest-neighbours within the corresponding sublattice.

3. Polarization

As discussed in Sec. I, nearest-neighbour eigenvector components are correlated in a propagon and uncorrelated in a diffuson/locon. To investigate the nature of nearest-neighbour vibrations in HEO, we project eigenvectors onto the unit sphere [26] according to

$$\varepsilon_\alpha(b; s) \rightarrow \frac{\varepsilon_\alpha(b; s)}{\sum_\alpha |\varepsilon_\alpha(b; s)|^2}. \quad (5)$$

Each dot in Fig. 6 (middle row) represents the arrowhead of a vector pointing in the direction along which a given atom oscillates. Observe that the polarizations in the leftmost column are not uniformly distributed over the unit sphere. This suggests correlated motion across the system, as expected in a propagon mode. In contrast, the 299 cm^{-1} and 622 cm^{-1} modes are incoherent with seemingly random distributions. This is consistent with the modes being diffusons or locons.

The polarizations in the $z = \frac{1}{2}$ plane are shown explicitly in the bottom row of Fig. 6. The z -component of each $\varepsilon_\alpha(b; s)$ has been suppressed for ease of visualization. Vortex-like structures appear in the propagon mode, indicating plane-wave-like character. The orientations in the 299 cm^{-1} and 622 cm^{-1} modes appear to be random.

4. Vortex density

The arrow plots of Fig. 6 show a few ‘vortex’ features in the low-energy modes. We argue that this can serve as a signature for plane-wave-like coherence. In a plane wave, the atomic-displacement-field varies in a smooth manner, akin to a flow-field. This smooth nature manifests as low

vorticity. In contrast, high-energy modes have displacements that vary drastically at the atomic scale. This leads to large vorticity – a large number of plaquettes (the squares formed by nearest-neighbour cation-oxygen bonds) have displacement fields that wind by $\pm 2\pi$. To formalize this argument, we define the ‘vortex density’ as

$$\rho_v(s) = \frac{1}{N_p} \sum_\ell \delta_{\theta_\ell, 2\pi} \quad (6)$$

where \sum_ℓ runs over the centers of the $N_p = 256$ plaquettes in the $z = \frac{1}{2}$ plane and θ_ℓ is the winding angle obtained by traversing the ℓ th plaquette counterclockwise [27]. The Kronecker delta picks out only the ‘up’-vortices; *i.e.* those vortices with curl directed out-of-the-page. It follows from Stokes’ theorem that up- and down-vortices are created in pairs [28].

The vortex density of Eq. 6 is plotted in Fig. 7 as a function of frequency. To interpret this result, we draw an analogy to the Berezinskii-Kosterlitz-Thouless (BKT) phase transition [28]. In an XY ferromagnet, low-temperature configurations are smooth with no vortices. In contrast, high-temperature configurations appear to be random with high vorticity. Here, we tune the energy of eigenmodes rather than temperature. At low energies, vorticity is non-zero, but small – indicating smoothness of the displacement field. As energy increases, vorticity grows indicating loss of coherence.

We propose that the eigenmodes transition from propagon- to diffuson-character via a crossover. The former are smooth with low vortex density while the latter have large vortex densities. We propose a heuristic criterion to locate the crossover: $\rho_v \sim 10\%$. As seen from Fig. 7, this criterion places the propagon-diffuson crossover at $\sim 200 \text{ cm}^{-1}$.

5. Spectral weight

It is worthwhile to investigate the plane-wave character of the eigenmodes. Following Allen *et al.* [9], we define the spectral weight associated with the mode s as

$$w_\alpha(q; s) = \left| \sum_b \varepsilon_\alpha(b; s) e^{iq \cdot b} \right|^2 \quad (7)$$

where $q_\alpha = 2\pi n_\alpha / Na$ is α th component of the wavevector, a is the average lattice constant calculated from the relaxed cell lengths in Table III, $N = 8$ is the number of times the conventional cubic unit cell was extruded along each Cartesian axis to generate the HEO supercell, and $n_\alpha = 0, 1, \dots, N_\alpha - 1$ are non-negative integers.

In Fig. 7 we plot $\sum_\alpha |w_\alpha(q; s)|^2$ for each of the allowed $\{q\}$ in three select eigenmodes. Only the $q = 0$ term contributes to Eq. 7 in the Goldstone mode. The propagon mode is a superposition of several plane waves with small q , while the diffuson modes contains contributions from many different $\{q\}$.

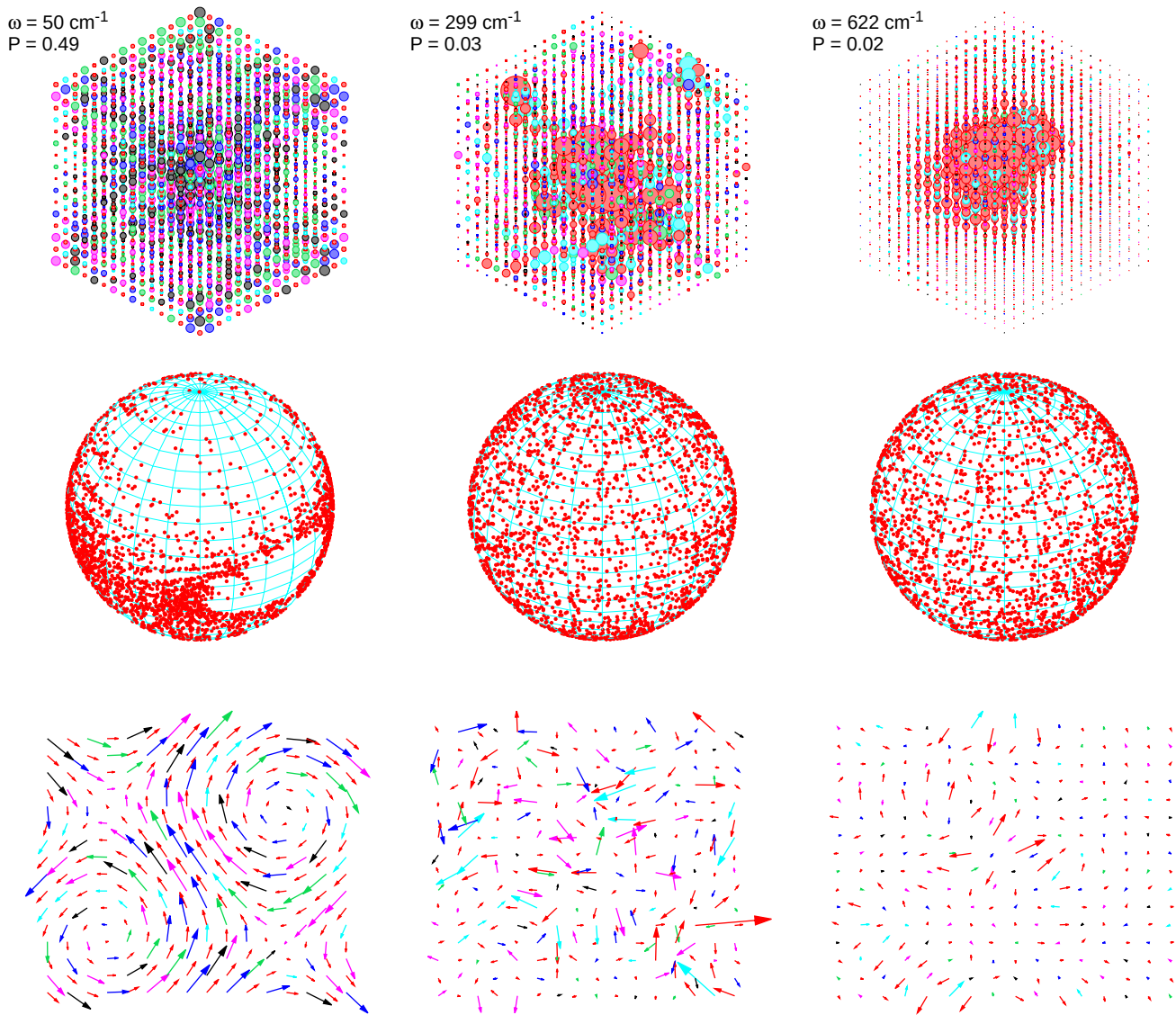


FIG. 6. (Top row): Spatial distribution of vibrational energy. A larger bubble indicates an atom which is vibrating more intensely. The atomic color scheme is defined in Fig. 4. (Middle row): Polarizations projected onto the unit sphere. (Bottom row): Polarizations in the $z = \frac{1}{2}$ plane. Mode frequencies and participation ratios (see Sect. III B 1) are listed in the upper left.

B. Localized vibrational modes

We next explore the possibility of localization in HEO by examining various diagnostics.

1. Participation ratio

The participation ratio P defined by

$$P(\omega_s) = \frac{1}{N} \times \frac{\left[\sum_b \sum_\alpha |\varepsilon_\alpha(b; s)|^2 \right]^2}{\sum_b \left[\sum_\alpha |\varepsilon_\alpha(b; s)|^2 \right]^2} \quad (8)$$

is an order parameter for Anderson localization in disordered systems. Here N is the number of atoms in the supercell. If in some mode, the vibration is localized on a single atom, then $P = N^{-1}$. Conversely, if all atoms contribute with equal weight to a mode, then $P = 1$. In practice, $P < 0.1$ is often used as the cutoff for localized modes [29]. We adopt a more conservative criterion for localization: $P < 0.05$.

Figure 9 compares the participation ratios of single 4096-atom disorder realizations of HEO, HESO, and HETeO. Each system has a mobility edge near 600 cm^{-1} beyond which P falls rapidly towards zero.

We find modes with $P < 0.05$ in two regions: in the middle of the spectrum at around 300 cm^{-1} and at the top end near 600 cm^{-1} . The low- P modes near

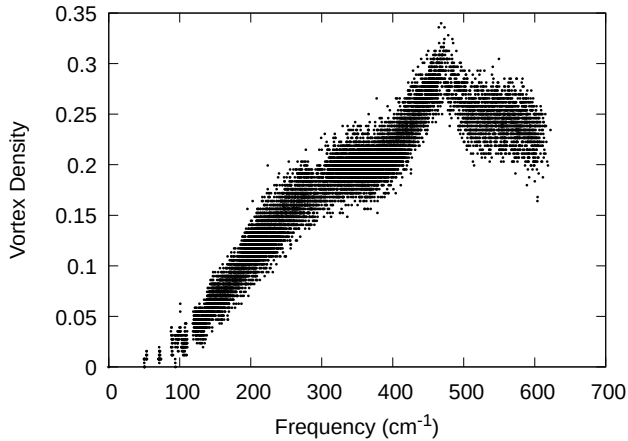


FIG. 7. Vortex density of polarizations in the $z = \frac{1}{2}$ plane.

300 cm^{-1} may originate from the transition from cation- to oxygen-dominated motion seen in the relative amplitudes (Fig. 4). Further support for this idea comes by noting that the relative amplitude of sulfur ions in HESO (Fig. 10) reaches a global maximum at 300 cm^{-1} . Hence there is no well-defined transition from cation- to oxygen-dominated motion in HESO, and hence no dip in its participation ratio.

In HETeO, the 300 cm^{-1} minimum is considerably wider and contains modes with very low ($P \sim 10^{-3}$) participation ratios. This phenomenon of localized mid-spectrum modes can be understood with reference to the parent oxide NiO. It has two phonon bands, separated by a band gap [30]. In broad terms, the lower and upper bands have acoustic and optical character, respectively. Upon introducing disorder, we may view each band as developing an independent mobility edge above which excitations are localized. In this point of view, the localized modes around 300 cm^{-1} are ‘acoustic locons’ while those near 600 cm^{-1} are ‘optical locons’.

2. Spatial distribution of vibrational energy

In the top row of Fig. 6, each ion in a 4096-atom disorder realization of HEO is represented by a sphere with diameter proportional to $\sum_{\alpha} |\varepsilon_{\alpha}(b; s)|^2$. Thus a larger sphere indicates an ion which is vibrating more intensely, and vice-versa. Periodic boundary conditions have been invoked to shift the atom b with the largest $\sum_{\alpha} |\varepsilon_{\alpha}(b; s)|^2$ to the center of the supercell. Visual inspection suggests that the 50 cm^{-1} and 299 cm^{-1} modes are extended, while the 622 cm^{-1} mode is localized.

Figure 12 shows the distribution of vibrational energy in a 299 cm^{-1} mode in HETeO. It appears that this mode is considerably more localized than the 299 cm^{-1} mode in HEO.

3. Local atomic environment

It is natural to ask whether or not short-range correlations influence the formation of the 620 cm^{-1} locon in Fig. 6. We denote the oxygen ion with the largest eigenvector component in the highest-frequency mode as $(\text{O})_{max}$. Figure 13 shows the distribution of n th nearest-neighbour cations surrounding $(\text{O})_{max}$. The distribution was averaged over fifty 4096-atom disorder realizations. There is a strong preference for Mg ions as nearest-neighbours. By the fifth nearest-neighbour shell ($\sqrt{5}a/2 \sim 4.7 \text{ \AA}$ away from $(\text{O})_{max}$), the distribution is practically uniform. Physically, the locon is situated in a cage of lighter Mg ions. There must then be a surplus of Zn and heavier cations at distances from $(\text{O})_{max}$ greater than the fifth nearest-neighbour shell, which insulate the vibration from the rest of the supercell. The nearest-neighbour bond lengths surrounding $(\text{O})_{max}$ were also investigated, but were equal within error to the bulk results in Table IV.

4. Localization length

Allen *et al.* [9] observed that the eigenvector components of a locon in α -Si decay according to

$$|\varepsilon(b; s)| \propto \exp\left(-\frac{|b - b_{max}|}{\xi_s}\right) \quad (9)$$

where b_{max} is the atom with the largest eigenvector component and ξ_s is the localization length of mode s , which should be much smaller than the size of the supercell. The decay profiles of three modes in a 4096-atom disorder realization of HEO are shown in Figure 14. The 622 cm^{-1} mode is well-described by Eq. 9 for all space and is localized within $\xi = 2.3(2) \text{ \AA}$. Neither the 299 cm^{-1} nor the 400 cm^{-1} modes agree well with Eq. 9. This is particularly surprising for the 299 cm^{-1} mode, which should be a locon according to its low participation ratio. Allen *et al.* have observed similar decay profiles for 590 cm^{-1} diffusons in α -Si [9].

Figure 15 shows the decay profile of the 299 cm^{-1} mode in HETeO depicted in Figure 12. Visual inspection suggests Figure 15 may be well-described by a double-exponential fit; *i.e.* this mode is a superposition of two locons; one with very small ξ near 0 \AA , and a second locon with larger ξ persisting over longer distances.

5. Level statistics

The level spacing ϵ_s between adjacent squared eigenfrequencies (*i.e.* eigenvalues of the dynamical matrix) is defined as $\epsilon_s = \omega_{s+1}^2 - \omega_s^2$. The level spacing ratio r_s is in turn defined as $r_s = \epsilon_s / \epsilon_{s-1}$. Random matrix theory predicts that the $\{r_s\}$ of an extended system in the Gaussian Orthogonal Ensemble are distributed according

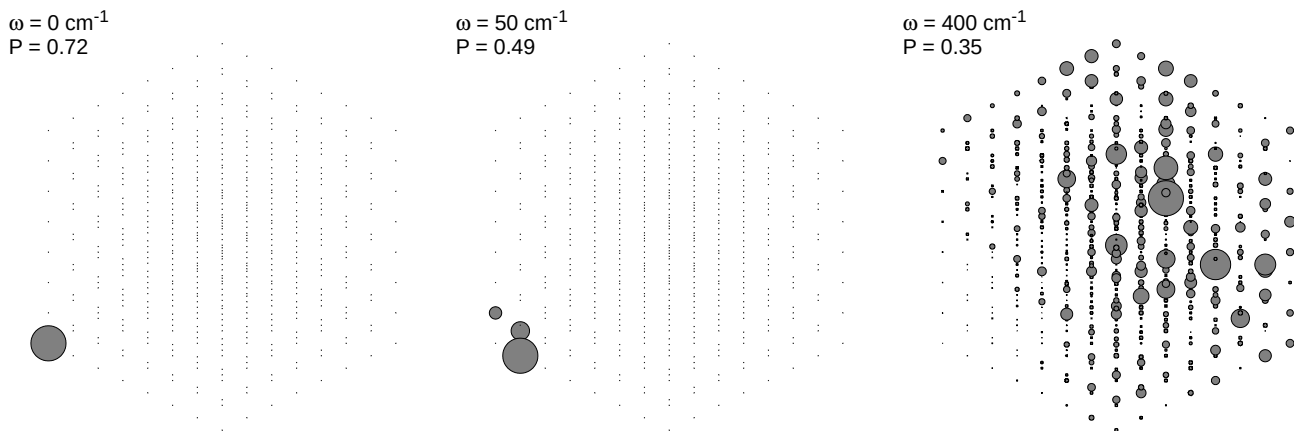


FIG. 8. Spectral weight on each atom in select eigenmodes. In all cases, the diameter of the largest bubble has been normalized to unity for ease of visualization.

to

$$P(r) = \frac{27}{8} \frac{r + r^2}{(1 + r + r^2)^{5/2}}, \quad (10)$$

while for a localized system the distribution is [31]

$$P(r) = \frac{1}{(1 + r)^2}. \quad (11)$$

Figure 16 shows the distribution of level spacing ratios for several frequency windows in HEO. An average was performed over fifty 4096-atom disorder realizations. As expected, the diffusons near 147 cm^{-1} and 400 cm^{-1} are well-described by Eq. 10. The level statistics also suggest that modes near 300 cm^{-1} are delocalized despite satisfying $P < 0.05$. This is consistent with the analysis of the localization lengths in Sec. III B 4. No range of frequencies could be found which resulted in an agreement between Eq. 9 and modes beyond the mobility edge. This may be due to a paucity of data points: each 4096-atom disorder realization contains only $\mathcal{O}(10^0)$ high-frequency locons, compared to $\mathcal{O}(10^3)$ diffusons between $350\text{--}400 \text{ cm}^{-1}$.

6. Correlation amplitude

We propose that localized and extended modes can further be differentiated by monitoring the time evolution of a vibrational wavepacket. Consider a cubic supercell C_1 of HEO wrapped in the center of a larger HEO environment \bar{C}_1 . The union of $C_1 \cup \bar{C}_1$ defines a larger supercell C_2 . If C_1 is not too small, C_2 should not look too dissimilar from periodic repetitions of C_1 . Now, suppose all the atoms in C_2 have zero initial velocity at time $t = 0$. Furthermore, let all the atoms in C_1 be displaced according to one of the eigenmodes of C_1 , and let all the atoms \bar{C}_1 be fixed to zero initial displacement. This defines a

wavepacket (consisting of the atoms in C_1) initially having potential energy only.

In analogy with quantum dynamics, it is possible to define, following Allen and Kelner [32], a correlation amplitude $C(t)$ for a wavepacket of HEO. This quantity represents the overlap of an initial local wavepacket (with deviations from equilibrium localized in a small region) with the evolved state at a later time. The details are left to the Appendix. The result is

$$C(t) = (\Omega^T \varepsilon^\dagger \mathbf{s})^T e^{-i\Omega t} (\Omega^T \varepsilon^\dagger \mathbf{s}) \quad (12)$$

where Ω is a diagonal matrix of the C_2 eigenfrequencies, ε is a unitary matrix of the C_2 eigenvectors, and \mathbf{s} is a column vector with components equal to zero if an atom $b \in \bar{C}_1$, and equal to a component of a C_1 eigenvector if $b \in C_1$. If the wavepacket consisted of locons, the wavefront should not spread far and the state of C_2 at a later time $t > 0$ should strongly resemble the initial state at time $t = 0$; *i.e.* the ratio $|C(t)/C(0)|$ of the correlation amplitudes should not deviate far from unity. Conversely, a wavepacket composed of propagons or diffusons should spread over C_2 and $|C(t)/C(0)|$ should decay to zero.

These predictions were tested by embedding a 1728-atom cluster of HEO in an 8000-atom environment. It may be seen in Figure 17 that the 617 cm^{-1} mode (the highest-frequency locon in C_1) remains very close to unity at all times, while the other modes decohere quickly.

IV. SUMMARY AND DISCUSSION

The experimental crystal structure, bond lengths, and optical conductivity of HEO are well-reproduced by modelling the ions as charged shells interacting through the Buckingham potential. We ascribe the weak mode in the optical conductivity discovered by Afsharvosoughi and

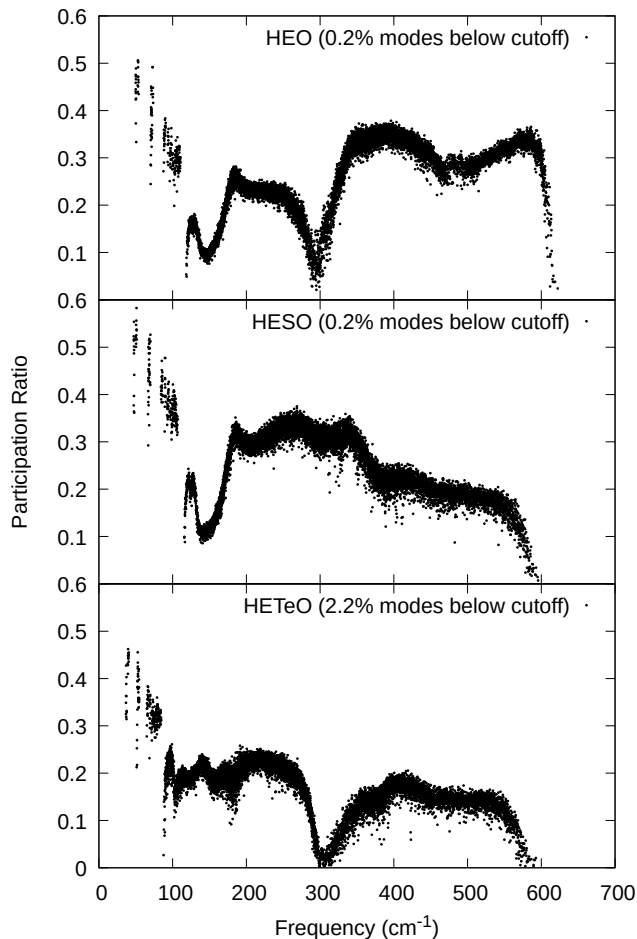


FIG. 9. Participation ratio of HEO, HESO, and HETeO.

Crandles to low-frequency, acoustic-like vibrations of Zn ions against a stationary oxygen sublattice. The combination of participation ratio, mode polarizations, localization length, and correlation amplitude suggest localized modes exist in HEO around 620 cm^{-1} , beyond a mobility edge. Modes in the vicinity of the transition from cation- to oxygen-dominated motion at 300 cm^{-1} have a tendency to localize, as reflected in low values of the participation ratio. Indeed, they may be driven to localize by increasing the mass disorder in the oxygen sublattice, as in the proposed HETeO.

Future studies, with larger system sizes, may find sharper signatures of localization. For example, it may be possible to reproduce the Wigner-Dyson and Poisson statistics (Eqs. 10 and 11) expected from theoretical considerations. This may require specialized numerical techniques such as the kernel polynomial method [33] to handle large matrices. Future studies may also be able to distinguish between propagons and diffusons by quantifying the spatial spread of energy. Propagons are expected to spread with a ballistic front, while diffusons are expected to spread diffusively.

Localized vibrational modes in HEO may be exper-

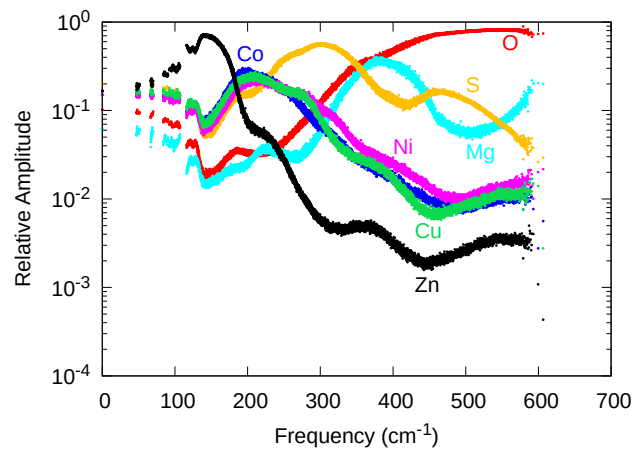


FIG. 10. Relative amplitudes in HESO.

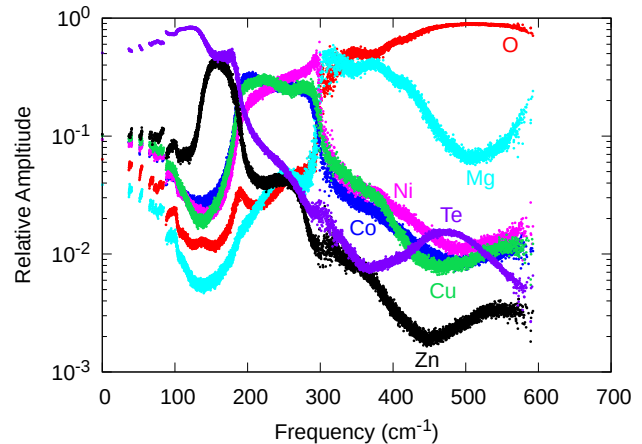


FIG. 11. Relative amplitudes in HETeO.

imentally observable by monitoring the spatial dependence of IR transmission. According to the participation ratio, a 300 cm^{-1} IR beam will excite diffusons. Sweeping the beam across a sample of HEO should not have a significant effect on the transmitted intensity. However, the transmitted intensity of 620 cm^{-1} light should plummet whenever the beam impinges upon a locon. Such an experiment will require small spot sizes that are comparable to typical locon mode radii. Recent advances with MINIFLUX nanoscopy [34] have achieved spot sizes as small as 1-3 nm – a few times larger than the locon in Fig. 14.

We have shown that admixing tellurium with oxygen to form HETeO creates mid-frequency localized modes. This can motivate synthesis efforts to increase entropy in the anion sublattice as well. The effects of mass and force constant disorder can further be studied in medium-entropy oxides [2], where the configurational entropy is considerably reduced, or in other high-entropy oxides with different crystal structures. Finally, the localization

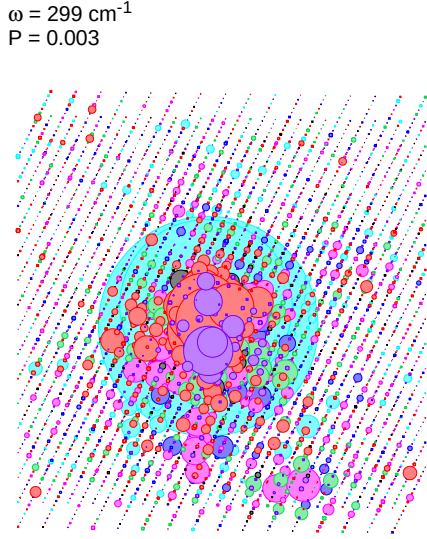


FIG. 12. Spatial distribution of vibrational energy in a 299 cm^{-1} mode in HETeO. The atomic color scheme is defined in Fig. 11.

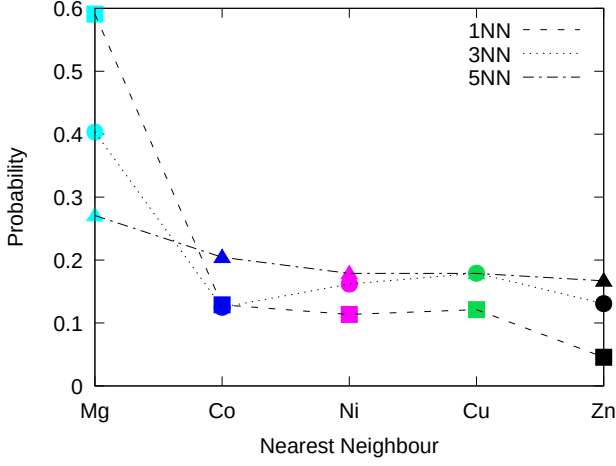


FIG. 13. Nearest-neighbours of the oxygen ion with the largest eigenvector component in the high-frequency mode. The dashed lines are guides to the eye.

of vibrations in HEO motivates future investigations into localization with other types of excitations. For example, neutron scattering studies have demonstrated that HEO develops antiferromagnetic order at $T \sim 112 \text{ K}$ [35]. The magnetic collective excitations share many similarities to the vibrational modes studied in this work. It is conceivable that high entropy oxides may host localized spin wave modes. We may find analogous localization with electronic states as well, *e.g.* in the related family of high entropy alloys [11].

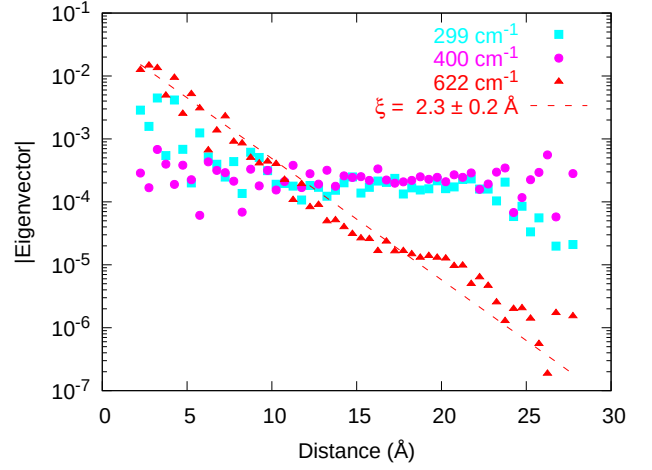


FIG. 14. Spatial decay of vibrational eigenvector components. The 622 cm^{-1} mode is localized within $\xi = 2.4(3) \text{ \AA}$.

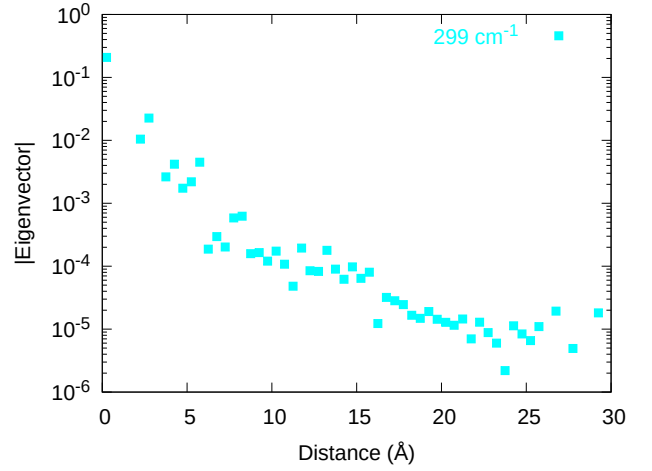


FIG. 15. Spatial decay of vibrational eigenvector components in 299 cm^{-1} mode in HETeO.

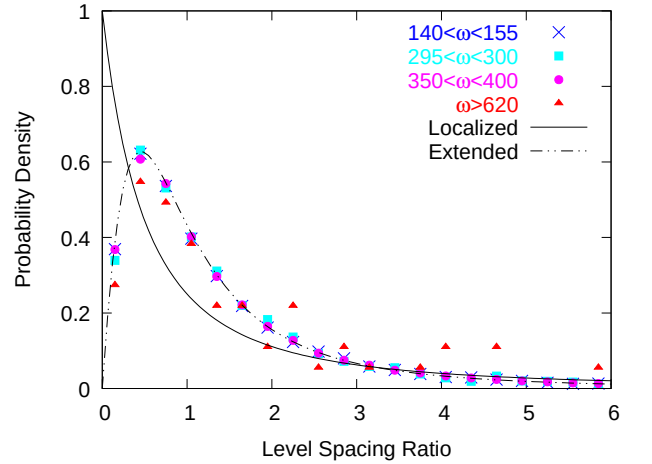


FIG. 16. Distributions of level spacing ratios. All frequencies are in units of cm^{-1} . The extended and localized distributions refer to Eqs. 10 and 11, respectively.

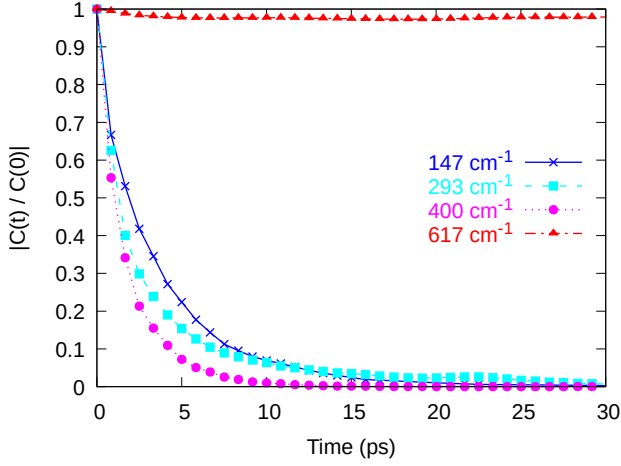


FIG. 17. Correlation amplitudes of select modes in HEO.

ACKNOWLEDGMENTS

This research was supported by the National Science and Engineering Council of Canada (NSERC) and the Ontario Provincial Government (QEII-GSST). We would like to thank Dr. Eric de Giuli (Toronto Metropolitan University), Dr. Jiri Hlinka (Czech Academy of Sciences), and Dr. Edward Sternin (Brock University) for their many useful comments and discussions.

Appendix A: Wavepacket Dynamics

The general, time-dependent solution $u_\alpha(\ell b; t)$ to the equations of motion in a crystal with \mathcal{N} unit cells is [25]

$$u_\alpha(\ell b; t) = \frac{1}{\sqrt{\mathcal{N}m_b}} \sum_{qs} Q(qs; t) \varepsilon_\alpha(b; qs) e^{iq \cdot \ell} \quad (\text{A1})$$

where ℓ labels the unit cells, m_b is the mass of the b th atom, q is one of the wavevectors allowed by periodic boundary conditions, and $\{Q\}$ are the normal coordinates defined by

$$Q(\ell b; t) = Q(qs; 0) \cos \omega_{qs} t + \frac{\dot{Q}(qs; 0)}{\omega_{qs}} \sin \omega_{qs} t. \quad (\text{A2})$$

$$\langle b\alpha | u(t) \rangle = \sum_{ss'} \sum_{b'\alpha'} \sum_{b''\alpha''} \sum_{b'''\alpha'''} \langle b\alpha | \hat{M}^{-\frac{1}{2}} | b'\alpha' \rangle \langle b'\alpha' | s \rangle \langle s | \hat{C}(t) | s' \rangle \langle s' | b''\alpha'' \rangle \langle b''\alpha'' | \hat{M}^{\frac{1}{2}} | b'''\alpha''' \rangle \langle b'''\alpha''' | u(0) \rangle. \quad (\text{A5})$$

Summations $\sum_s |s\rangle\langle s|$ or $\sum_{b\alpha} |b\alpha\rangle\langle b\alpha|$ over dyads generate resolutions of unity by completeness. Hence Eq. A5 can be succinctly written as

$$|u(t)\rangle = \hat{M}^{-\frac{1}{2}} \hat{C}(t) \hat{M}^{\frac{1}{2}} |u(0)\rangle \quad (\text{A6})$$

By substituting Eq. A2 into Eq. A1 and exploiting the completeness and orthonormality of the vibrational eigenvectors $\{\varepsilon_\alpha(b; qs)\}$, it is possible to express the initial $\{Q, \dot{Q}\}$ in terms of the initial $\{u, \dot{u}\}$:

$$Q(qs; 0) = \frac{1}{\sqrt{\mathcal{N}}} \sum_{b\alpha} \sqrt{m_b} \varepsilon_\alpha^*(b; qs) \times \sum_{\ell} u_\alpha(\ell b; 0) e^{-iq \cdot \ell}. \quad (\text{A3})$$

An identical equation holds with Q replaced by \dot{Q} and u replaced by \dot{u} . Consider now the application of the foregoing equations to a large supercell. To first approximation the Brillouin zone consists of the single point $q = 0$; *i.e.* converged phonon properties are obtained from a Γ -point calculation only. From this it follows that $\ell = 0$ and $\mathcal{N} = 1$. Substituting Eqs. A2 and A3 into Eq. A1 produces

$$u_\alpha(b; t) = \frac{1}{\sqrt{m_b}} \sum_s \varepsilon_\alpha(b; s) \cos \omega_s t \times \sum_{b'\alpha'} \sqrt{m_{b'}} \varepsilon_{\alpha'}^*(b'; s) u_{\alpha'}(b'; 0) \quad (\text{A4})$$

where the labels $\ell = q = 0$ have been discarded. The Dirac notation used by Allen and Kelner [32] is now introduced through the correspondence rules

$$\begin{aligned} u_\alpha(b; t) &\leftrightarrow \langle b\alpha | u(t) \rangle \\ \varepsilon_\alpha(b; s) &\leftrightarrow \langle b\alpha | s \rangle \\ \varepsilon_\alpha^*(b; s) &\leftrightarrow \langle s | b\alpha \rangle \\ \cos \omega_s t \delta_{ss'} &\leftrightarrow \langle s | \hat{C}(t) | s' \rangle \\ m_b \delta_{bb'} \delta_{\alpha\alpha'} &\leftrightarrow \langle b\alpha | \hat{M} | b'\alpha' \rangle \end{aligned}$$

Here $\{m_b\}$ are the eigenvalues of the mass operator \hat{M} which is diagonal in the direct space basis $\{|b\alpha\rangle\}$. Similarly, $\{\cos \omega_s t\}$ are the eigenvalues of the operator $\hat{C}(t)$ which is diagonal in the eigenbasis $\{|s\rangle\}$. It is easily shown that Eq. A4 can be recast as

where we have used the fact that Eq. A4 holds for an arbitrary bra vector $\langle b\alpha |$. Similarly, for the velocities

$$|v(t)\rangle = -\hat{M}^{-\frac{1}{2}} \hat{\Omega} \hat{S}(t) \hat{M}^{\frac{1}{2}} |u(0)\rangle \quad (\text{A7})$$

where $\hat{\Omega}$ and $\hat{S}(t)$ are diagonal in the eigenbasis with eigenvalues $\{\omega_s\}$ and $\{\sin \omega_s t\}$, respectively. Following Allen and Kelner, consider now the vector

$$\begin{aligned} |W(t)\rangle &= \hat{M}^{\frac{1}{2}} |v(t)\rangle - i\hat{\Omega}\hat{M}^{\frac{1}{2}} |u(t)\rangle \\ &= e^{-i\hat{\Omega}t} |W(0)\rangle \end{aligned} \quad (\text{A8})$$

where used has been made of Eqs. A6 and A7. Since Eq. A8 has the same form as the Schrödinger equation for state kets, with $e^{-i\hat{\Omega}t}$ playing the role of the time evolution operator, it follows that $|W(t)\rangle$ is the classical analogue of the quantum state of the system. Taking the overlap of $|W(t)\rangle$ with $|W(0)\rangle$ gives the formula for the correlation amplitude shown in Eq. 12.

-
- [1] C. M. Rost, E. Sachet, T. Borman, A. Moballegh, E. C. Dickey, D. Hou, J. L. Jones, S. Curtarolo, and J.-P. Maria, Entropy-stabilized oxides, *Nature Communications* **6**, 8485 (2015).
- [2] T. Afsharvosoughi and D. A. Crandles, An infrared study of antiferromagnetic medium and high entropy rocksalt structure oxides, *Journal of Applied Physics* **130**, 184103 (2021).
- [3] M. R. Chellali, A. Sarkar, S. H. Nandam, S. S. Bhattacharya, B. Breitung, H. Hahn, and L. Velasco, On the homogeneity of high entropy oxides: An investigation at the atomic scale, *Scripta Materialia* **166**, 58 (2019).
- [4] J. L. Braun, C. M. Rost, M. Lim, A. Giri, D. H. Olson, G. N. Kotsonis, G. Stan, D. W. Brenner, J.-P. Maria, and P. E. Hopkins, Charge-induced disorder controls the thermal conductivity of entropy-stabilized oxides, *Advanced Materials* **30**, 1805004 (2018).
- [5] Q. Wang, A. Sarkar, D. Wang, L. Velasco, R. Azmi, S. S. Bhattacharya, T. Bergfeldt, A. Düvel, P. Heitjans, T. Brezesinski, H. Hahn, and B. Breitung, Multi-anionic and -cationic compounds: new high entropy materials for advanced Li-ion batteries, *Energy Environ. Sci.* **12**, 2433 (2019).
- [6] Y. M. Beltukov, C. Fusco, D. A. Parshin, and A. Tanguy, Boson peak and ioffe-regel criterion in amorphous siliconlike materials: The effect of bond directionality, *Phys. Rev. E* **93**, 023006 (2016).
- [7] R. J. Bell and D. C. Hibbins-Butler, Acoustic and optical modes in vitreous silica, germania and beryllium fluoride, *Journal of Physics C: Solid State Physics* **8**, 787 (1975).
- [8] P. B. Allen and J. L. Feldman, Thermal conductivity of disordered harmonic solids, *Phys. Rev. B* **48**, 12581 (1993).
- [9] P. B. Allen, J. L. Feldman, J. Fabian, and F. Wooten, Diffusons, locons and propagons: Character of atomic vibrations in amorphous si, *Philosophical Magazine B* **79**, 1715 (1999).
- [10] E. Abrahams, P. W. Anderson, D. C. Licciardello, and T. V. Ramakrishnan, Scaling theory of localization: Absence of quantum diffusion in two dimensions, *Phys. Rev. Lett.* **42**, 673 (1979).
- [11] J.-W. Yeh, S.-K. Chen, S.-J. Lin, J.-Y. Gan, T.-S. Chin, T.-T. Shun, C.-H. Tsau, and S.-Y. Chang, Nanostructured high-entropy alloys with multiple principal elements: Novel alloy design concepts and outcomes, *Advanced Engineering Materials* **6**, 299 (2004).
- [12] A. Carvalho, R. Jones, M. Sanati, S. K. Estreicher, J. Coutinho, and P. R. Briddon, First-principles investigation of a bistable boron-oxygen interstitial pair in Si, *Phys. Rev. B* **73**, 245210 (2006).
- [13] R. J. Bell and P. Dean, Atomic vibrations in vitreous silica, *Discuss. Faraday Soc.* **50**, 55 (1970).
- [14] J. D. Gale and A. L. Rohl, The General Utility Lattice Program (GULP), *Molecular Simulation* **29**, 291 (2003).
- [15] C. F. Tipaldi and J. Gabrusenoks, Lattice dynamics calculations for Mg_{1-x}Zn_xO solid solutions, *Latvian Journal of Physics and Technical Sciences* **59**, 3 (2022).
- [16] B. G. Dick and A. W. Overhauser, Theory of the dielectric constants of alkali halide crystals, *Phys. Rev.* **112**, 90 (1958).
- [17] G. V. Lewis and C. R. A. Catlow, Potential models for ionic oxides, *Journal of Physics C: Solid State Physics* **18**, 1149 (1985).
- [18] Lewis and Catlow assumed oxygen was polarizable and treated all cations with the rigid-ion model. Hence there were no dipole-dipole interactions and $C_{bb'} = 0$. The assumption here is that oxygen is larger and more polarizable than the cations in HEO and should therefore experience the largest dipole-dipole force.
- [19] V. N. Popov, Shell model parameters for layered copper oxides, *Journal of Physics: Condensed Matter* **7**, 1625 (1995).
- [20] L. Lin, K. Wang, R. Azmi, J. Wang, A. Sarkar, M. Botros, S. Najib, Y. Cui, D. Stenzel, P. Anitha Sukkurji, Q. Wang, H. Hahn, S. Schweidler, and B. Breitung, Mechanochemical synthesis: route to novel rock-salt-structured high-entropy oxides and oxyfluorides, *Journal of Materials Science* **55**, 16879 (2020).
- [21] G. Anand, A. P. Wynn, C. M. Handley, and C. L. Freeman, Phase stability and distortion in high-entropy oxides, *Acta Materialia* **146**, 119 (2018).
- [22] D. Berardan, A. Meena, S. Franger, C. Herrero, and N. Dragoë, Controlled Jahn-Teller distortion in (MgCoNiCuZn)O-based high entropy oxides, *Journal of Alloys and Compounds* **704**, 693 (2017).
- [23] J. Sushil, A. Kumar, A. Gautam, and M. I. Ahmad, High entropy phase evolution and fine structure of five component oxide (Mg, Co, Ni, Cu, Zn)O by citrate gel method, *Materials Chemistry and Physics* **259**, 124014 (2021).
- [24] C. M. Rost, Z. Rak, D. W. Brenner, and J.-P. Maria, Local structure of the Mg_xNi_xCo_xCu_xZn_xO (x=0.2) entropy-stabilized oxide: An exafs study, *Journal of the American Ceramic Society* **100**, 2732 (2017).
- [25] G. P. Srivastava, *The Physics of Phonons*, 1st ed. (Routledge, 1990).
- [26] Y. Yao, G. Ren, Y. Yu, J. Che, T. Liang, L. Li, Y. Liu, F. Yang, and X. Zhao, Thermal conduction mechanism of ferroelastic Zr-Y-Yb-Ta-Nb-O high-entropy oxides with glass-like thermal conductivity, *Journal of the American Ceramic Society* **105**, 4360 (2022).
- [27] G. Alvarez and H. Fort, Phase transitions driven by vortices in two-dimensional superfluids and superconductors: From kosterlitz-thouless to first order, *Phys. Rev.*

- B **63**, 132504 (2001).
- [28] U. Gerber, W. Bietenholz, and F. G. Rejón-Barrera, New insight into the Berezinskii-Kosterlitz-Thouless phase transition, *Journal of Physics: Conference Series* **651**, 012010 (2015).
- [29] H. R. Seyf and A. Henry, A method for distinguishing between propagons, diffusions, and locons, *Journal of Applied Physics* **120**, 025101 (2016).
- [30] W. Reichardt, V. Wagner, and W. Kress, Lattice dynamics of NiO, *Journal of Physics C: Solid State Physics* **8**, 3955 (1975).
- [31] Y. Y. Atas, E. Bogomolny, O. Giraud, and G. Roux, Distribution of the ratio of consecutive level spacings in random matrix ensembles, *Phys. Rev. Lett.* **110**, 084101 (2013).
- [32] P. B. Allen and J. Kelner, Evolution of a vibrational wave packet on a disordered chain, *American Journal of Physics* **66**, 497 (1998).
- [33] A. Weiße, G. Wellein, A. Alvermann, and H. Fehske, The kernel polynomial method, *Rev. Mod. Phys.* **78**, 275 (2006).
- [34] K. C. Gwosch, J. K. Pape, F. Balzarotti, P. Hoess, J. Ellenberg, J. Ries, and S. W. Hell, Minflux nanoscopy delivers 3d multicolor nanometer resolution in cells, *Nature Methods* **17**, 217 (2020).
- [35] J. Zhang, J. Yan, S. Calder, Q. Zheng, M. A. McGuire, D. L. Abernathy, Y. Ren, S. H. Lapidus, K. Page, H. Zheng, J. W. Freeland, J. D. Budai, and R. P. Hermann, Long-range antiferromagnetic order in a rocksalt high entropy oxide, *Chemistry of Materials* **31**, 3705 (2019).